Laser Writing of Electronic Circuitry in Thin Film Molybdenum Disulfide: a Transformative Manufacturing Approach

Drake Austin[a,b], Kimberly Gliebe[c], Christopher Muratore[d], Bryce Boyer[e], Timothy S. Fisher[e], Lucas Beagle[a,b], Anna Benton[a,d], Paige Look[a,d], David Moore[a,b], Emilie Ringe[f,g], Benjamin Treml[a], Ali Jawaid[a,b], Richard Vaia[a], W. Joshua Kennedy[a], Philip Buskohl[a], Nicholas R. Glavin[a]

[a]*Air Force Research Laboratory, Materials and Manufacturing Directorate, WPAFB, OH 45433, United States of America*

[b]*UES Inc., Dayton, OH 45432, United States of America*

[c]*Case Western Reserve University, Cleveland, OH 44106*

[d]*University of Dayton, Dayton, OH 45409*

[e]*University of California Los Angeles, Los Angeles, CA 90095*

[f]*Department of Materials Science and Metallurgy, University of Cambridge, Cambridge CB3 0FS, UK*

[g]*Department of Earth Sciences, University of Cambridge, Cambridge CB2 3EQ, UK*

Electronic circuits, the backbone of modern electronic devices, require precise integration of conducting, insulating, and semiconducting materials in two- and three-dimensional space to control the flow of electric current. Alternative strategies to pattern these materials outside of a cleanroom environment, such as additive manufacturing, have enabled rapid prototyping and eliminated design constraints imposed by traditional fabrication. In this work, a transformative manufacturing approach using laser processing is implemented to directly realize conducting, insulating, and semiconducting phases within an amorphous molybdenum disulfide thin film precursor. This is achieved by varying the incident visible (514 nm) laser intensity and raster-scanning the thin film *a*-MoS_2 sample (900 nm thick) at different speeds for micro-scale control of the crystallization and reaction kinetics. The overall result is the transformation of select regions of the *a*-MoS_2 film into MoO_2, MoO_3, and 2H-MoS_2 phases, exhibiting conducting, insulating, and semiconducting properties, respectively. A mechanism for this precursor transformation based on crystallization and oxidation is developed using a thermal model paired with a description of the reaction kinetics. Finally, by engineering the architecture of the three crystalline phases, electrical devices such as a resistor, capacitor, and chemical sensor were laser-written directly within the precursor film, representing an entirely transformative manufacturing approach for the fabrication of electronic circuitry.

1. Introduction

The microscale deposition, patterning, and manipulation of thin film materials into precisely controlled device architectures remains arguably the most important advancement in creating electronic circuitry found in modern electronics. The development of device fabrication techniques including photolithography, reactive ion etching, and physical vapor deposition aggressively accelerated the first demonstration of the integrated circuit in 1958 [1,2] where current state of the art feature sizes within device elements are now approaching the atomic scale [3]. The device elements (e.g. resistors, capacitors, diodes, and transistors) within these circuits rely on controlled electron transport within three basic building blocks of electronic materials: insulators, conductors, and semiconductors. It is only through the precise integration of these three subsets of materials that electronics as we know them today are realized.

Revolutionary materials within each of these three categories have helped shape the field of modern electronics, including silicon, III-V semiconductors, oxide dielectrics, and others. Transition metal dichalcogenides (TMDs), in particular, represent an emerging material class, with the two-dimensional monolayer form exhibiting an indirect to direct bandgap transition [4], strong spin-orbit coupling [5,6,7], excitonic behavior [8], and a reduced elastic modulus for mechanical flexibility [9,10]. Within the family of TMDs, diverse electronic properties are accessible for circuitry, from highly conductive TaS_2 to bandgaps in the visible range such as in monolayer MoS_2 and WS_2 (1.8 eV and 2.03 eV, respectively) [11]. The semiconducting properties exhibited by MoS_2 led to its integration within fully integrated multistage circuits composed of inverters, NAND gates, and static random access memory all on a single chip [12,13]. Additionally, researchers have developed unique strategies to phase-pattern the growth of two different phases of $MoTe_2$ (semiconducting 2H and conducting 1T') to construct high performance field effect transistors and other logic devices with only a single step process [14].

Transition metal oxides (TMOs) are another intriguing class of electronic materials, as the unique nature of the outer *d*-electrons and variable metal-oxygen bond strength from nearly ionic to highly covalent or metallic reveals a wealth of available electronic properties for future circuit designers [15]. This vast class of metal oxides encompasses metallic materials (RuO_2, ReO_3), highly insulative materials ($BaTiO_3$), and materials whose electronic properties are controlled by external environment or composition (V_2O_3, La_{1-x}, Sr_xVO_3). As such, the electronic properties of molybdenum oxides are highly dependent upon the crystal stoichiometry, which has been shown to be highly tunable via doping, oxygen vacancies, and morphology [16-19]. The most commonly observed oxide is MoO_3, which displays a wide bandgap of 3.0 eV and typical insulative properties. MoO_3 thin films can be deposited by vapor phase deposition, sol-gel processing, and thermodynamic oxidation of transition metal sulfides [20]. Less common is the electrically conductive MoO_2 phase, known to form as an intermediate oxide in MoO_3 formation from MoS_2 as well as in processing from molybdenum ore [21]. Both molybdenum (IV) and (VI) oxides have been investigated in conjunction with TMDs, to realize TMD/TMO interfaces with improved contact junctions and electronics with complex heterostructures [22-25].

Strategies to pattern electronic materials including TMDs and TMOs in unique ways outside of a cleanroom environment, such as additive manufacturing, can potentially allow for rapid device prototyping and remove many of the design constraints in traditional fabrication [26-29]. While

additive manufacturing exhibits challenges including reproducibility, ink stability, and others, the benefits of the accessible design space, low cost, and paradigm shift from traditional manufacturing are substantial. For instance, additive manufacturing has been demonstrated as a viable technique to realize fully printable microelectronic circuit elements operating as a passive wireless senor for various applications [30]. In this study, laser manufacturing approaches are leveraged to locally induce crystallization and oxidation of a monolithic thin film precursor, allowing for the manipulation of insulating, semiconducting, and conducting materials for the purpose of designing electronic circuitry on a single chip. This method represents neither an additive nor subtractive method, but rather a transformative manufacturing strategy using a laser to embed circuit devices including resistors, capacitors, and a gas sensor starting from a monolithic amorphous MoS_2 film. The lateral integration of semiconducting crystalline 2H-MoS_2, conducting MoO_2, and insulating MoO_3 via laser irradiation enabled device circuitry fabrication in air or inert environments at ambient pressure, without masking or photolithography steps.

2. Experimental methods

2.1 Sample fabrication

The samples consisted of 900 ± 20 nm thick films of amorphous MoS_2 (*a*-MoS_2) grown on 0.5 mm thick willow glass substrates by magnetron sputtering at a substrate temperature of 25°C. Sputtering was performed via asymmetric bi-polar pulsed direct current magnetron sputtering at 65 kHz (with a 0.4 s reverse time) from a polycrystalline MoS_2 target (Plasmaterials) at room temperature with a growth rate of approximately 1 atomic layer per second. While this technique has been previously used to grow ultra-thin films [31-33], the growth time was extended to 60 min in order to produce the thicker films. The 900 nm films were synthesized in order to minimize the effects ablation, improve the performance of the laser-written circuitry, and to minimize the influence of the substrate. Thinner films were also synthesized at a thickness of 6.5 nm (growth time 30 seconds) to elucidate the possibility of nanoscale films.

2.2 Laser processing

The output of an argon-ion laser (Coherent Innova 90C) with a central wavelength of 514 nm was focused onto the sample at normal incidence using a 20x magnification, infinity-corrected objective (Mitutoyo V80286315). The corresponding $1/e^2$ beam radius during processing was measured to be 44 ± 0.2 μm. The sample itself was housed in a home-built environmental control cell mounted on two high-precision, two-axis translation stages (Physik Instrumente M-687.UL and P-563.3CD). The sample was translated in conjunction with the operation of an optical shutter (Thorlabs SHB025T) to control exposure of the surface to the laser beam. For a Gaussian beam, the on-target intensity (power density) as a function of the Cartesian position on the sample *x*, *y* and time *t* can be described by

$$I(x,y,t) = I_0 \exp\left(-2\frac{(x-vt)^2+y^2)}{w^2}\right) \qquad (1)$$

where I_0 is the peak intensity, v is the translation velocity (taken to be in the x-direction), and w is the beam radius. For a point at the origin, this intensity is equivalent to that of a static, temporally Gaussian laser pulse with a full width at half maximum (FWHM) pulse duration of $t_{eff} = \sqrt{(2\ln 2)}w/v$ referred to here as the effective exposure time. By varying the stage velocity and laser power, this effective exposure time can be controlled along with the peak intensity. In order to determine the effect these two parameters have on the modification of the sample in air, a grid of lines was written with powers varying from 20-400 mW (spaced linearly) and translation speeds from 10^{-2}-10^{1} mm/s (spaced logarithmically). The corresponding intensities and exposure times spanned ranges of 0.66-13.2 kW/cm^2 and 5 - 5000 ms.

2.3 Sample analysis

Transformation of the precursor phase was characterized via Raman spectroscopy, photoluminescence spectroscopy, and X-ray photoelectron spectroscopy (XPS). Unless otherwise stated, all Raman spectra were taken at the geometric centers of each laser-modified region. When creating large regions of laser-exposed material for XPS or conductivity analysis, a series of lines were written by raster-scanning the sample with a center-to-center line separation of 10 μm. This value was empirically found – through Raman and XPS analysis – to maximize conversion of the region while minimizing undesired, additional annealing of prior traces. Electrical characterization including resistance and capacitance measurements were carried out using a four-point probe station (Cascade Microtech MPS150-B1A). Resistance uncertainties were based on the standard deviation of 20 repeated measurements (including probe lift-off and touch-down) along with the uncertainty of the probe separation, sample thickness, and laser-written line width, where appropriate.

Scanning electron microscope (SEM) and atomic force microscope (AFM) images were also taken to determine the polycrystallinity and topography of the laser-irradiated regions in comparison to the untreated sample. Scanning microwave microscopy (SMM) was used to spatially map the dielectric properties of the laser-written material with sub-micron precision. Optical spectroscopy using transmitted white light illumination was performed with a MicroExtinction Spectroscopy (MExS) setup described in Ref. [34].

2.4 Gas sensor characterization

Prior to gas sensor testing, the sample was placed in a 2.2 L stainless steel chamber which was flushed overnight with dry nitrogen. The sample was put in series with a 1 MΩ reference resistor and a bias of 1 V was applied. All voltages were applied and measured with a data acquisition system (Measurement Computing USB 1808X) at a resolution of 18 bits (±5 V range). Voltages

were acquired at a rate of 200 kHz, and each grouping of 40,000 points was averaged and stored. A mixture of 1000 ppm NH_3 balanced with nitrogen (Indiana Oxygen) was mixed with dry nitrogen using mass flow controllers (MKS Instruments 1179C series) to produce the desired concentration (1:99 for 10 ppm, 1:9 for 100 ppm, and unmixed for 1000 ppm). The total flow of the NH_3 plus nitrogen was 2000 sccm.

3. Results and discussion

3.1 Structure and composition of laser-irradiated precursor material

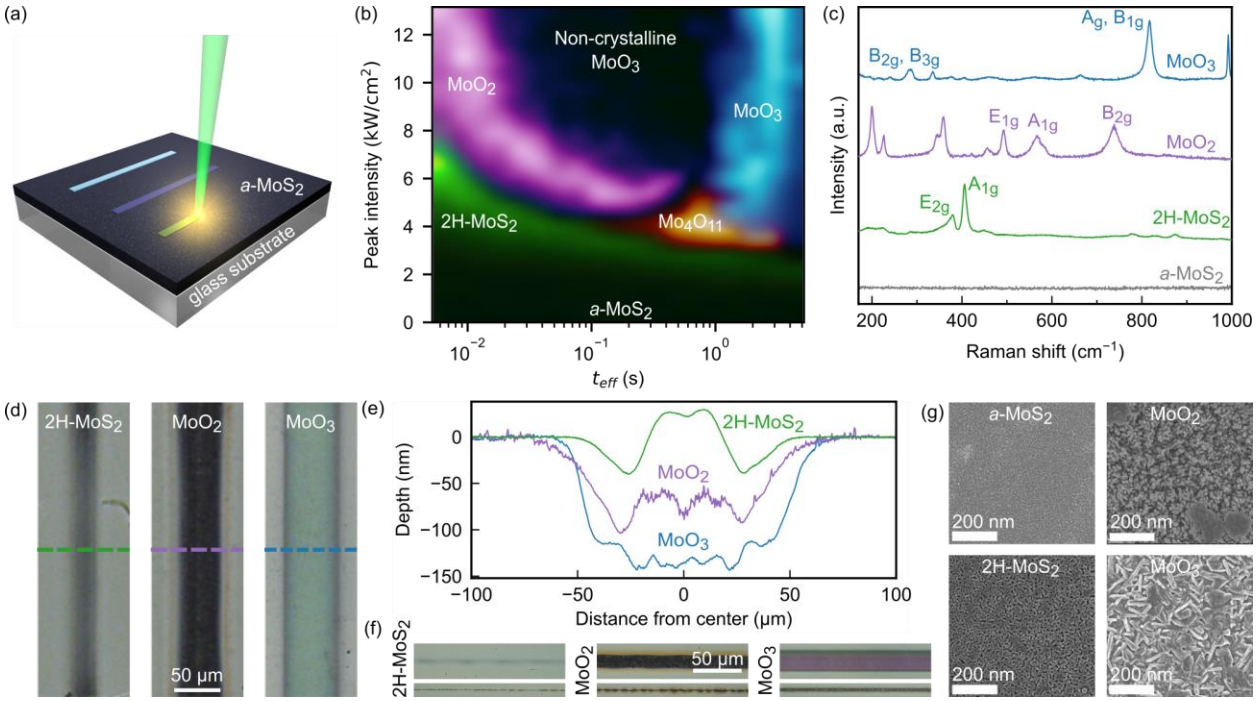

Figure 1 (a) Schematic of the laser-writing process. (b) Phase map illustrating the laser intensities and exposure times at which each of the three phases are observed to form. The color intensities shown are determined by overlaying and interpolating the plots of the normalized Raman signals shown in Fig. S2(a). (c) Raman spectra measured for 2H-MoS_2 (3.3 kW/cm^2, 5 s), MoO_2 (8.5 kW/cm^2, 5 ms), and MoO_3 (6.6 kW/cm^2, 5 ms). (d) Confocal microscope images of each phase. Peak intensities and exposure times: 9.2, 9.2, and 6.6 kW/cm^2 and 5 s, 5 ms, 5 ms for MoO_3, MoO_2, and 2H-MoS_2, respectively. (e) AFM profiles across each phase. (f() Confocal microscope images of each phase written with 10 and 2 μm focal spot sizes. g) SEM images of each phase, as well as the untreated a-MoS_2.

Exposure of a 900nm thick *a*-MoS_2 thin film on a glass substrate to 514 nm wavelength, continuous-wave laser light (schematically depicted in Fig 1(a)) resulted in the formation of distinct chemical phases. By varying the peak laser intensity and exposure time while the sample was exposed to lab air, a processing map depicted in Fig. 1(b) was created, revealing the formation of four distinct regions of crystalline 2H-MoS_2, MoO_2, Mo_4O_{11}, and MoO_3. The color intensities shown are determined by overlaying and interpolating the plots of the normalized Raman peak intensities (Fig. S2(a)) for distinct peaks associated with each phase (A_{1g}, B_{2g}, and A_{1g} for MoO_3, MoO_2, and 2H-MoS_2, respectively and the Raman peak at 907 cm^{-1} for Mo_4O_{11}). A key feature to note in Fig. 1(b) is the separation between the three phases in this parameter space. While the

formation of 2H-MoS_2 and MoO_2 can be seen over a wide range of exposure times, they require lower intensities at the higher exposure times and are most readily formed at the lowest exposure times (~ milliseconds). In contrast, the MoO_3 phase is only seen at longer exposure times (~ seconds), with the Mo_4O_{11} phase forming as an intermediate between MoO_2 and MoO_3 (corresponding to MoO_{3-x} for x=0.25). Additionally, within their optimal exposure time values, the formation of the three oxides occurs after crossing an intensity threshold; below this intensity, only crystalline 2H-MoS_2 is present.

For the purposes of this study, the primary focus will be on the 2H-MoS_2, MoO_2, and MoO_3 phases, as they represent an exciting opportunity for vastly different accessible electronic properties. The full Raman spectra for these three phases at select optimized intensity and exposure time values are plotted in Fig. 1(c), indicating distinct crystal structure with no evidence of mixing. Optical images of each phase are shown in Fig. 1(d), along with AFM profiles showing the changes in the sample height after laser exposure (Fig. 1(e)). Notably, a reduction in thickness is observed in the formation of oxide films due to partial film ablation. The MoO_3 films exhibited a greater loss in thickness relative to MoO_2 even though the density is lower for the trioxide than the dioxide (6.47 g/cm^3 for MoO_2 as compared to 4.69 g/cm^3 for MoO_3). This indicates that the two orders of magnitude longer exposure (annealing) time required to form the MoO_3 phase is primarily contributing to the loss of material and is a design consideration going forward.

Crystallization into 2H-MoS_2 and oxidation into MoO_2 is also possible with much thinner films (e.g. 2D films). By increasing the laser intensity in order to compensate for decreased absorption and increased thermal losses, such phase transitions were observed with a 6.5 nm *a*-MoS_2 film (Fig. S3(b)). Oxidation into MoO_3, however, was not observed due to ablation, which was likely a result of sublimation given that the MoO_3 sublimes readily at the temperatures required for its formation [35] (see thermal modeling results in the next section). While this sublimation leaves the majority of the thicker films left, this is not the case for few-layer films and further optimization will be required to reveal the chemical and structural phases seen in these 900 nm films.

A significant benefit of the laser writing process over other manufacturing techniques is in the versatility with regards to the feature size. While Fig. 1(d) depicts laser-written lines is on the order of 50 μm (for w_0 = 44 μm), smaller lines of each phase can be readily formed simply by reducing the focal spot size and adjusting the stage velocity. This is shown in Fig. 1(f) where confocal microscope images of lines of 2H-MoS_2, MoO_2, and MoO_3 are compared for focal spot sizes of w_0 = 10, and 2 μm (see Fig. S2(d) for plots of the corresponding Raman signals). With the smallest focal spot, a lateral resolution of 2 μm is achieved, and it is expected that higher resolutions are achievable with smaller focal spots. In addition, flat-top beam profiles and selective choice of thermally conductive substrates could be used to further localize the boundary of each transformed region and further push the resolution of the laser writing technique into the nanoscale.

To further elucidate the nanoscale structure of the phases, SEM images shown in Fig. 1(g) reveals a nanocrystalline homogenous crystal structure. This is further revealed in high-resolution AFM images (Fig. S5) with nanocrystals on the order of 100 nm in size observed for the MoO_2 and MoO_3 phases. The 2H-MoS_2 depict nanocrsytals with grain sizes observed on the order of 50 nm.

3.2

Fundamental formation mechanisms

The formation of the thermodynamically stable MoO_3 is to be expected, as it forms by heating crystalline MoS_2 to >300 ^oC in the presence of oxygen [36-39]. Less clear is the formation of MoO_2 at shorter exposure times. However, studies of the oxidation of molybdenite found MoO_2 to be a reaction intermediate [40,41] with the reaction described by

$$\mathrm{MoS_2} + 3\,\mathrm{O_2} \longrightarrow \mathrm{MoO_2} + 2\,\mathrm{SO_2} \qquad (2)$$

$$2\,\mathrm{MoO_2} + \mathrm{O_2} \longrightarrow 2\,\mathrm{MoO_3} \qquad (3)$$

Given the observation of MoO_2 formation at short exposure times (where rapid quenching may occur), it is proposed here that MoO_2 similarly exists as a reaction intermediate in the oxidation of highly disordered *a*-MoS_2, with the oxidation into MoO_3 occurring at a much slower rate. During the shorter exposure times, the sample is quenched and the reaction halted before the oxidation of MoO_2 into MoO_3 (or the Mo_4O_{11} intermediate) can occur. Even so, higher temperatures (and, therefore, higher intensities) are needed to ensure that the reaction rate is high enough for oxidation into MoO_2 to occur within the ~1 ms timescales. Otherwise, 2H-MoS_2 forms alongside the MoO_2, eventually becoming the dominant product of the laser-writing process, as observed at the lower intensities where only chemical rearrangement occurs. This has previously been observed in few-layer *a*-MoS_2 and *a*-WS_2 films where the formation mechanism was shown to be a kinetically-controlled photothermal effect [42]. Oxidation of MoO_2 into MoO_3 through laser irradiation has also been observed by Dieterle *et al.* [43], albeit with significantly longer exposure times and lower intensities.

In order to lend further support to this argument, the thermal aspects of the laser-writing process were considered. With the laser intensity acting as a heat source, the experimental conditions are modeled using the 3D heat equation

$$\rho c_p \frac{\partial T}{\partial t} = \nabla \cdot (k \nabla T) - \frac{1}{d} H(z)\,(1 - H(z-d)) \times \left[\sigma\varepsilon(T^4 - T_{amb}^4) + AI(x,y,t)\right] \qquad (4)$$

where T is the temperature, T_{amb} is the ambient temperature, σ is the Stefan-Boltzmann constant, d is the film thickness, I is the incident laser intensity given by Eq. (1), H is the Heaviside step function, and ρ, c_p , k, ε, and A are the material's density, specific heat capacity, thermal conductivity, surface emittance, and absorptance at the laser wavelength, respectively. The heating from the laser is assumed to be uniform throughout the thickness of the film; this is justified as the characteristic time for thermal diffusion in the transverse dimension is given by $t_{D,\perp} \sim d^2/\alpha \sim$20 ns [44] for a thermal diffusivity of α=4.9×10^{-5} m^2/s, which is significantly shorter than any other timescales under consideration. Eq. (4) was solved numerically using the COMSOL finite element analysis software, modeling the sample as a film of *a*-MoS_2 on a silica substrate – both with a temperature-dependent thermal conductivity and specific heat capacity. Radiative losses were

accounted for by treating the top surface as a diffuse emitter with an emissivity of 0.6. Specific details of the model can be found in the supplementary material.

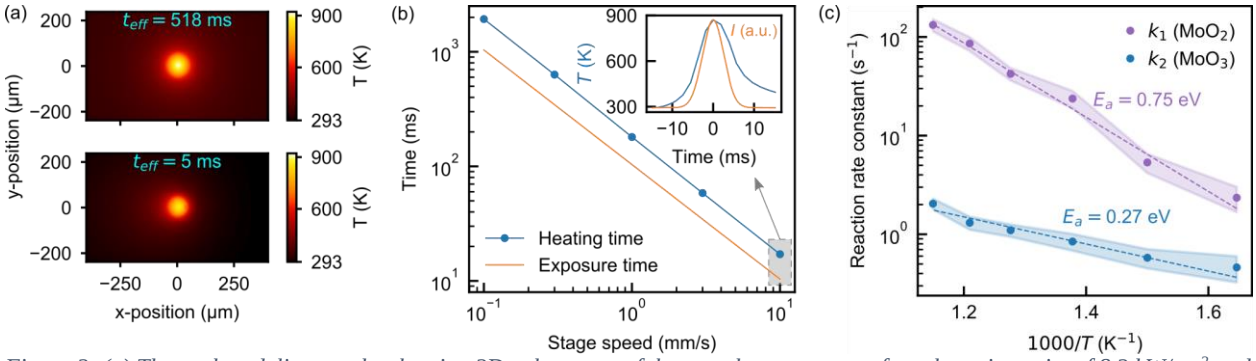

Figure 2: (a) Thermal modeling results showing 2D color maps of the sample temperature for a laser intensity of 8.2 kW/cm^2 and exposure times of 518 and 5 ms. (b) Exposure time and characteristic heating time as a function of stage speed. Inset: temperature at the center of the simulated region as a function of time for a stage speed of 10 mm/s (t_{eff}=5 ms). The laser intensity profile is also plotted for comparison. The FWHM of the temperature profile is used to determine the heating time for all speeds. (c) Fitted values of the reaction rate constant for both steps of the reaction as a function of T^{-1}. Arrhenius fits are also shown, together with the resulting activation energies.

Example 2D color maps of the thermal modeling results are shown in Fig. 2(a) with exposure times of 518 and 5 ms at an intensity of 8.2 kW/cm^2 . These results show that the heated region is approximately twice the size of the laser spot, with a small rise in the temperature of the surrounding material. Additionally, the exposure time is seen to have little effect on the peak temperature, suggesting that the equilibrium temperature is quickly reached (see also Fig. S7(b) where the peak temperature is plotted as a function of intensity for a range of exposure times). Consequently, the thermal effects of intensity and exposure time can largely be decoupled, with the intensity governing the temperature of the irradiated region, and the exposure time governing the duration spent at that temperature. This can be analyzed more closely by considering the temperature of a point at the center of the simulated region as the beam passes. An example plot of this temperature as a function of time is shown in the inset of Fig. 2(b) for t_{eff} = 5 ms where the temperature rises and falls with the passing of the laser beam. The characteristic heating time is determined from the FWHM of this temperature profile and is plotted as a function of stage speed along with the corresponding exposure times. This heating time is approximately twice that of t_{eff}, where the broadening is due to a rise in temperature of the surrounding material. Given that the heating time decreases in step with the exposure time, it is concluded that thermal diffusion is not a limiting factor in the quench time. This is to be expected given that the characteristic time for lateral thermal diffusion is $t_{D,\parallel} \sim w^2/\alpha \sim 40$ μs, appreciably shorter than all values of t_{eff} investigated. In other words, the irradiated region on the sample can be considered quenched and the oxidation process halted after the laser has passed. If values of t_{eff} close to or less than $t_{D,\parallel}$ were to be used, the heating time could potentially be limited by $t_{D,\parallel}$, depending on the thermal conductivity of the substrate. Overall, these results are very similar to those of Bell *et al.* [45], where microsecond heating times were achieved with various samples on a Si substrate.

With these insights from the thermal model, a more detailed analysis of the reaction kinetics can be performed. The two-step reaction can be described by the rate equations

$$\frac{\mathrm{d}C_{\mathrm{MoS_2}}}{\mathrm{d}t} = -k_1 C_{\mathrm{MoS_2}} \quad (5)$$

$$\frac{\mathrm{d}C_{\mathrm{MoO_2}}}{\mathrm{d}t} = k_1 C_{\mathrm{MoS_2}} - k_2 C_{\mathrm{MoO_3}} \quad (6)$$

$$\frac{\mathrm{d}C_{\mathrm{MoO_3}}}{\mathrm{d}t} = k_2 C_{\mathrm{MoO_3}} \quad (7)$$

where C is the concentration of the appropriate compound and k_1 and k_2 are the reaction rate constants for the reactions described by Eqs. (2) and (3), respectively. The temperature dependence of these reaction constants can be modeled using the Arrhenius equation

$$k_1 = A_1 \exp\left[-E_{a,1}/k_b T\right] \quad (8)$$

$$k_2 = A_2 \exp\left[-E_{a,2}/k_b T\right] \quad (9)$$

where A_1 and A_2 are the corresponding Arrhenius constants, $E_{a,1}$ and $E_{a,2}$ are the activation energies, k_b is Boltzmann's constant, and T is the temperature of the irradiated region. These rate equations can be solved analytically if the reaction rate constants are treated as time-independent, i.e. if the temperature profile is modeled as constant over the duration of the heating time. Under the assumption that the Raman intensity for MoO_2 in the phase map (Figs. 1(b) and S2(b)) is proportional to the concentration of MoO_2, a fit was performed using the solutions to Eq. (6) with the rate constants as fitting parameters. This was performed at intensities ranging from 3.3-6.6 kW/cm^2, where the peak of the MoO_2 signal could be clearly identified. Using the thermal model results (Fig. S7(b)), the temperatures corresponding to these intensities were identified. The resulting plot of the rate constants as a function of T^{-1} is shown in Fig. 2(c), with the shaded regions representing the uncertainty of the fit for each data point (±1 standard deviation determined from the sum of square residuals) . These were further fitted to Eqs. (8) and (9), yielding activation energies of $E_{a,1}$ = 0.75 ± 0.04 eV and $E_{a,2}$ = 0.27 ± 0.04 eV. For comparison, Marin *et al.* [40] reports activation energies of 0.23 eV for both steps of the reaction, and argues that O_2 diffusion into the bulk is limited by the flow of SO_2 while MoO_2 is forming. It is therefore likely that the thickness of the film results in a diffusion-controlled reaction rate and a correspondingly higher activation energy. In other words, oxidation in the bulk of the film is inhibited by the outflow of SO_2 until MoO_2 formation is complete. This suggests that surface oxidation is likely still occurring in the 2H-MoS_2 region of the phase diagram, which is visually apparent in the optical image of the 2H-MoS_2 line in Fig. 1(d). This line is noticeably darker than the surrounding *a*-MoS_2, a feature that is not present when processing in high purity argon.

3.3 Material property characterization

The laser writing process results in uniform crystal structure within the exposed region, with some evidence of a transition region in the periphery, as shown in Fig. 3(a) where a 2D Raman map was taken for a representative spectral line of each phase. From these images, it is clear that the Raman signals correspond to the visual changes observed optically. It is worth noting, however, that the

periphery of the MoO_2 line shows an appreciable 2H-MoS_2 signal, likely due to the lower intensity in this region from the Gaussian beam profile and diffusive heating. As shown in Fig. 3(c), there is a process window (~8-10 kW/cm^2) in which a mixed phase of MoO_2 and 2H-MoS_2 can form. SMM images provide additional evidence for the formation of 2H-MoS_2 at the edges of MoO_2 lines (Fig. S11). Interestingly, the MoO_3 line shows oscillations in Raman intensity due to oscillations in the stage velocity at low speeds, which can be minimized with more stage optimization and highlights the need for precise control of exposure time.

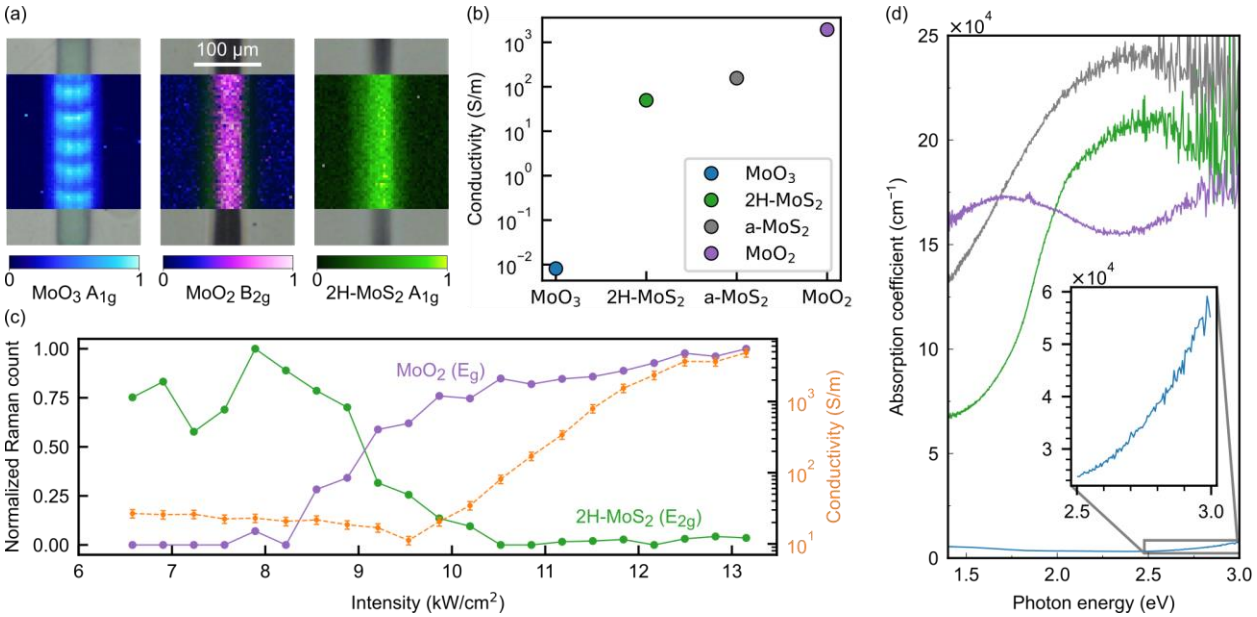

Figure 3 (a) 2D color maps of the Raman intensity associated with the predominant Raman peak of each phase. Each image is an overlay of the signal for all three peaks, i.e. the colorbars apply to each image. (b) Conductivity of large, (5mm)^2 regions of each phase from four-point sheet resistance measurements. The standard deviations are 9, 7, 12, and 3% for MoO_3, 2H-MoS_2, a-MoS_2, and MoO_2, respectively representing the error in several consecutive measurements along with the uncertainties in the film thickness. (c) Plot of the conductivity of individual lines as a function of laser intensity for an exposure time of 5 ms, along with the normalized Raman signal for the MoO_2 and 2H-MoS_2 E_g and E_{2g} peaks. (d) Absorption spectra for each phase.

To evaluate the suitability of each phase transformed from the amorphous MoS_2 precursor material, the longitudinal electrical conductivity of each phase was determined using a four-point probe method. Large (5 mm)^2 regions of each phase were written by raster-scanning the laser at an intensity of 9.2 kW/cm^2 with exposure times of 5 s for the MoO_3 phase and 5 ms for the MoO_2 and 2H-MoS_2 phases. The corresponding peak temperatures predicted by the thermal model are 700 and 650°C. In the case of 2H-MoS_2, the sample was processed in argon to prevent oxidation of the overlapping traces. The sheet resistances were then measured with a ~100 μm probe separation and found to be 0.8, 7.1, and 21.4 kΩ/□ for MoO_2, *a*-MoS_2, and 2H-MoS_2, respectively, and 170MΩ/□ for MoO_3. The thicknesses of each respective region were measured with a profilometer to be 670, 900, 940, and 725 ± 20 nm. The corresponding conductivities are shown in Fig. 3(b) with standard deviations of 9, 7, 12, and 3% for MoO_3, 2H-MoS_2, *a*-MoS_2, and MoO_2, respectively. Additionally, the conductivity of the 2H-MoS2 phase demonstrated an increase in conductivity with elevated temperatures, demonstrating the expected semiconducting properties of the phase (Fig. S12). The MoO_3 phase shows a relatively low conductivity of 8.1× 10^{-3} S/m, similar to the value of ~10^{-3} S/m reported in Ref. [46]. This relatively insulating behavior compared

to the other phases allows the MoO_3 phase to be used for electrical isolation of the 2H-MoS_2 and MoO_2 phases, with leakage currents <1% at the currents tested (1-2 μA). With this method of isolation, the longitudinal conductivity of the 2H-MoS_2 and MoO_2 phases were measured for individual lines written with varying intensities and a fixed exposure time of 5 ms. A plot of the line conductivity as a function of peak laser intensity is shown in Fig. 3(c), with the normalized Raman signals associated with each phase plotted as well. A sharp transition from the 2H-MoS_2 to MoO_2 phase is observed with a slight lag in conductivity values, presumably corresponding to a more crystalline MoO_2 phase. The purest 2H-MoS_2 and MoO_2 phases show conductivities of 25 S/m and 4.8×10^3 S/m, respectively. For comparison, reported values for *a*-MoS_2 include 11 S/m [32] and 22 S/m [47], similar to the amorphous and crystalline values for MoS_2 reported here. The conductivity of MoO_2, in contrast, has been reported to be 1.2×10^6 S/m [48], approximately two orders of magnitude larger than the value reported here. This indicates room for improvement of the oxide chemistry and polycrystallinity. It is also worth noting that these conductivities represent an averaging over the width of the isolated line, as the purity of the phase varies over this width (Fig. 3(a)). It should be emphasized, however, that the ability to locally switch between the 2H-MoS_2 and MoO_2 phases on a single chip is the primary benefit of this technique for device applications, and that a continuum of material properties can be accessed by varying the processing conditions.

Absorption coefficients of the different phases were evaluated using Micro-extinction Spectroscopy (MExS) [34] and depicted in Fig. 3(d), assuming thicknesses corresponding to the AFM profiles for each phase. The optical spectra reveal bandgaps of 1.65 eV and 2.69 eV for 2H-MoS_2 and MoO_3, respectively; no clear bandgap is observed for MoO_2, indicating that it is metallic. For comparison, Refs. [4] and [49] report 1.29 and 2.85 eV for MoS_2 and MoO_3, respectively. The higher bandgap measured here for 2H-MoS_2 is possibly due to surface oxidation, while the lower bandgap measured for MoO_3 is likely due to some degree of sub-stoichiometricity. In addition to bandgap values, indication as to the extent of crystalline conversion can be evaluated using these spectra. The MoO_3 absorption coefficient at a wavelength of 514 nm was measured to be 3.2×10^3 cm^{-1} for a corresponding optical penetration depth of 3.1 μm – reasonably close to the bulk values of 2.3×10^3 cm^{-1} and 4.3 μm reported for MoO_3 [50]. As MoS_2 and MoO_2 are opaque to visible light with optical penetration depths of ~60 nm, this indicates that the oxidation into MoO_3 is complete throughout the depth of the film. This is further supported by the observed transparency of the transformed MoO_3 regions while AFM scans showed a height difference of only 130 nm relative to the surrounding *a*-MoS_2. In the cases of 2H-MoS_2 and MoO_2, the optically apparent changes are visible on the back side of the sample, suggesting that their formation also extends through the depth of the film. This is to be expected in particular for 2H-MoS_2, given that its formation is a thermally-induced chemical rearrangement (as evidenced by the increase in film thickness after annealing) rather than a chemical reaction, and that the film thickness ensures uniform heating through the depth of the film. In order to provide further evidence for the formation of each phase through the depth of the film, Raman scans were taken from the back side of the sample through the transparent substrate, indicating that significant crystallization and oxidation is able to extend to the bottom of the film (see Fig. S4).

4. Electronic circuit devices

With the ability to create isolated regions of conducting (MoO_2), semiconducting (2H-MoS_2), and insulating (MoO_3) patterns, fabrication of circuit elements becomes possible. By connecting these elements with laser-written lines of conducting MoO_2, simple devices can be made. The simplest circuit element to make is a resistor. While the MoO_2 phase is conducting, it can be made relatively resistive due to the 800 nm film thickness (after processing) and by using a less pure phase of MoO_2. By raster-scanning lines in a serpentine pattern, a resistor (inset of Fig. 4(a)) was written with an intensity of 8.9 kW/cm^2 and an exposure time of 5 ms. This intensity is slightly lower than the optimized conditions for peak conductivity in MoO_2 to enable a detectable change in resistance, further highlighting the ease in which the circuitry can be designed and optimized. In order to prevent current leakage through the *a*-MoS_2, the perimeter of the serpentine was traced with an insulating line of MoO_3. The corresponding plot of resistance as a function of serpentine length is shown in Fig. 4(a). The resistance increases linearly with length, as it would for a conventional resistor. Similarly, capacitors can be written with varying plate areas governed by the film thickness and the overlapping line length. A plot of the measured capacitance as a function of the total overlapping line length per comb is shown in Fig. 4(b), for both parallel-plate and comb capacitors. The MoO_3 phase can also be used to better isolate the capacitor plates, while simultaneously serving as a dielectric to further increase the capacitance to over 1 pF with a 9% coefficient of variation, comparable to similarly dimensioned comb capacitors patterned using photolithography [51]. An image of such a capacitor with six "tines" is shown in the inset of Fig. 4(b).

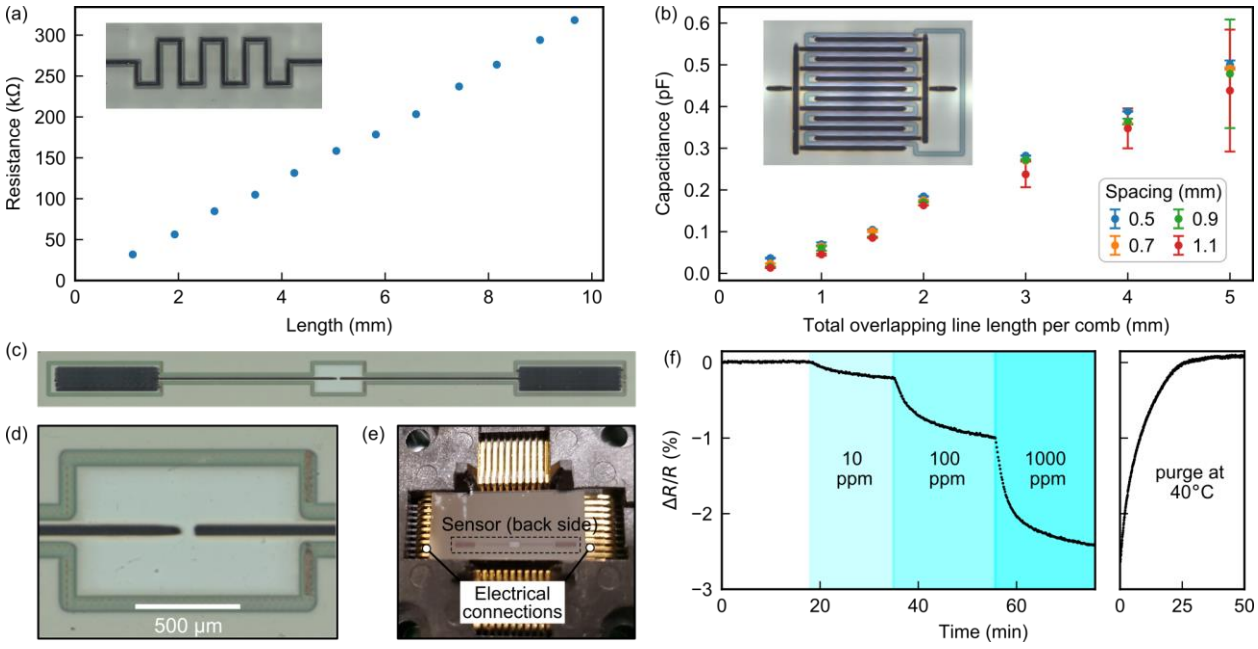

Figure 4 (a) Resistance of a laser-written serpentine resistor as a function of length, where the perimeter of the serpentine was traced with MoO_3 to provide electrical isolation. The error associated with the measurement was between 1.1 and 1.5 kΩ, (b) Capacitance of a series of laser-written parallel-plate and comb capacitors as a function of overlapping line length per comb. (c) Confocal microscope image of a laser-written gas sensor using MoO_2 for contact pads and electrical connections, MoO_3 for

isolation, and 2H-MoS_2 for the sensing region. (d) Zoom-in of (c) showing the sensing region and the 70 μm gap between electrical connections in the center. (e) Image of the gas sensor placed within a clamshell-style test socket. (f) Plot of the relative change in sensor resistance $\Delta R/R$ as a function of time. At specific moments in time, varying concentrations of NH_3 are introduced, which modulates the resistivity of the 2H-MoS_2 region. The recovery of the sensor during N_2 purging at 40°C is also shown.

Active circuit elements incorporating semiconducting elements allow for architectural engineering of electronic building blocks for more complex circuit elements. In this case, chemical gas sensors utilizing the semiconducting 2H-MoS_2 phase as the sensing region, the MoO_2 phase as electrical contacts and wires, and the insulating MoO_3 phase for isolation were fabricated solely through laser transformation of the *a*-MoS_2 precursor phase. Such a sensor is shown in Fig. 4(c)-(e), where two MoO_2 contacts are separated by a 70 μm gap within a 1.0 × 0.6 mm region of 2H-MoS_2. This 2H-MoS_2 region was written with an intensity of 9.2 kW/cm^2 and a 5 ms exposure time in an argon ambient environment to reduce oxidation of the sample during processing. Fig. 4(f) shows the response of the sensor to 10, 100, and 1000 ppm of NH_3, which modulates the conductivity of the 2H-MoS_2 via electron donation upon adsorption. A clear change in resistance above the noise level can be seen for each NH_3 concentration, indicating a clear sub-10 ppm detection limit of NH_3. The recovery of the sensor during N_2 purging at 40°C can also be seen, with full recovery due to desorption achieved after 25 min. The intrinsic 1/e response time at 10 ppm is approaching 6.8 minutes and 8.5 minutes for heated recovery time, matching similar responses found in nanoscale devices of MoS_2.

While monolayer or few-layer MoS_2–based sensors have reported sub 0.1 ppm detection of NH_3 gas, the sub 10 ppm detection of NH_3 exhibited herein is sufficiently below the 50 ppm threshold from the US Occupational Safety and Health Administration (OSHA) for limited short term exposure.[54] It is expected that an increase in sensitivity to gaseous species can be achieved by reducing the precursor film thickness to increase the surface-area-to-volume ratio, as well as by further process optimization. As addressed previously, careful consideration to balancing ablation processes upon reduction of the film thickness is necessary to ensure formation of the higher temperature oxide phases. Additionally, while a simple geometry was used for this sensor, the unique ability to create such devices from an inexpensive, naturally-abundant precursor material through laser-writing and without any other patterning or photolithography steps allows for multiple sensors optimized for varying functionalities to be rapidly produced on a single chip.

5. Conclusions

In summary, it has been shown that thin-film *a*-MoS_2 can be locally transformed into polycrystalline 2H-MoS_2, MoO_2, and MoO_3 through laser-induced phase and chemical transformation. Each of these phases require specific laser intensities and exposure times to form, as MoO_2 and MoO_3 phases were found to form most readily at intensities near 10 kW/cm^2 with exposure times on the order of milliseconds and seconds, respectively. In air, the 2H-MoS_2 phase formed most readily at lower intensities of 6.5 kW/cm^2 with millisecond exposure times. Thermal simulations indicate that laser-induced heating occurs on microsecond time scales and can lead to localized temperatures exceeding 1000°C. By translating the sample during processing, the duration spent at these temperatures for any given region can be varied from milliseconds to

seconds, which in turn controls the reaction kinetics of the oxidation process, resulting in conversion to either MoO_3 or its reaction intermediate MoO_2. At lower temperatures and exposure times, oxidation is minimized and photothermal crystallization results instead. These 2H-MoS_2, MoO_2, and MoO_3 phases were shown to extend over the width of the treated region and through the depth of the film, allowing them to exhibit the necessary semiconducting, conducting, and insulating electrical properties, respectively.

The approach to creating electronic devices including resistors, capacitors, and gas sensors by purely transformation of an initial starting film represents a very advantageous manufacturing strategy. Further optimization of film uniformity utilizing different laser sources and profiles (i.e. flat top vs. Gaussian) is expected to result in highly controllable properties for future electronics and sensor devices. Additionally, exploring the transformative manufacturing technique utilizing optical sources to include flash lamps, parallel laser sources, laser holography, and pulsed laser systems will significantly reduce the manufacturing time and increase throughput as compared to the CW laser utilized in this study [55-57]. The tradeoff between simplicity of configuration and desire for throughput will determine the optical source required in future transformative manufacturing systems, with potentially portable units taking advantage of the CW setup described herein and more complicated sources (i.e. flash lamp or pulsed laser setup) requiring more extensive infrastructure. In addition to the manufacturing speed and high throughput for a laser system, another advantage is in the reconfigurability of the process. By simply modifying the laser pattern, individual electronic circuits can be designed on the fly with nearly complete freedom within the bounds of the manufacturing process. This is in contrast to traditional circuit design using thin film cleanroom processes, which can restrict reconfigurability, requires expensive start-up equipment, and a multitude of both additive and subtractive steps to complete. In this simple, elegant solution, the amorphous film and a laser is all that is required to drive the necessary patterning and local electronic property control needed for functional devices. Thus, we refer to this process as transformative manufacturing, where – following the initial thin film deposition – the entire circuit design is driven by the laser writing of embedded TMD and TMO phases. The amorphous film is non-participative in the final design and while there is potentially some small amount of ablation, the resultant devices are merely transformations of this starting material. It is expected that by laser-processing these, or similar, materials in active gases, many different chemical reactions can be locally induced, possibly with the ability to access other reaction intermediates and more complex circuitry.

Funding Sources

This research was funded in part by the Air Force Office of Scientific Research under grant number FA9550-20RXCOR057. E.R. acknowledges funding from the Air Force Office of Scientific Research under grant No. AFOSR-YIP FA9550-17-1-0202.

Supporting Information

Supporting information is included to accompany this manuscript with laser characterization, Raman spectroscopy maps, AFM scans, thermal simulation data, X-Ray photoelectron spectroscopy scans, MExS results, and SMM scans.

Data Availability

The raw and processed data required to reproduce these findings are available by request to the corresponding author.

References

[1] J. S. Kilby, Invention of the integrated circuit, IEEE Transactions on electron devices 23 (7) (1976) 648-654, doi:https://doi.org/10.1109/T-ED.1976.18467.

[2] J. S. Kilby, Miniaturized electronic circuits, US Patent 3,138,743, 1964, doi: https://doi.org/10.1109/N-SSC.2007.4785580.

[3] S. B. Desai, S. R. Madhvapathy, A. B. Sachid, J. P. Llinas, Q. Wang, G. H. Ahn, G. Pitner, M. J. Kim, J. Bokor, C. Hu, et al., MoS2 transistors with 1- nanometer gate lengths, Science 354 (6308) (2016) 99-102, doi:https://doi.org/10.1126/science.aah4698.

[4] K. F. Mak, C. Lee, J. Hone, J. Shan, T. F. Heinz, Atomically thin MoS2: a new direct-gap semiconductor, Physical review letters 105 (13) (2010) 136805, doi: https://doi.org/10.1103/PhysRevLett.105.136805.

[5] A. Kormányos, V. Zólyomi, N. D. Drummond, G. Burkard, Spin-orbit coupling, quantum dots, and qubits in monolayer transition metal dichalcogenides, Physical Review X 4 (1) (2014) 011034, doi: https://doi.org/10.1103/PhysRevX.4.011034.

[6] D. Xiao, G.-B. Liu, W. Feng, X. Xu, W. Yao, Coupled spin and valley physics in monolayers of MoS 2 and other group-VI dichalcogenides, Physical review letters 108 (19) (2012) 196802, doi: https://doi.org/10.1103/PhysRevLett.108.196802.

[7] B. T. Zhou, K. Taguchi, Y. Kawaguchi, Y. Tanaka, K. Law, Spin-orbit coupling induced valley Hall effects in transition-metal dichalcogenides, Communications Physics 2 (1) (2019) 1-7, doi: https://doi.org/10.1038/s42005-019-0127-7.

[8] R. P. Chaudhary, S. Saxena, S. Shukla, Optical properties of stanene, Nanotechnology 27 (49) (2016) 495701, doi:https://doi.org/10.1088/0957-4484/27/49/495701.

[9] W. Zhu, S. Park, M. N. Yogeesh, D. Akinwande, Advancements in 2D flexible nanoelectronics: From material perspectives to RF applications, Flexible and Printed Electronics 2 (4) (2017) 043001, doi: https://doi.org/10.1088/2058-8585/aa84a4.

[10] D. Akinwande, N. Petrone, J. Hone, Two-dimensional flexible nanoelectronics, Nature communications 5 (1) (2014) 1-12, doi:https://doi.org/10.1038/ncomms6678.

[11] X. Duan, C. Wang, A. Pan, R. Yu, X. Duan, Two-dimensional transition metal dichalcogenides as atomically thin semiconductors: opportunities and challenges, Chemical Society Reviews 44 (24) (2015) 8859- 8876, doi:https://doi.org/10.1039/C5CS00507H.

[12] H. Wang, L. Yu, Y.-H. Lee, Y. Shi, A. Hsu, M. L. Chin, L.-J. Li, M. Dubey, J. Kong, T. Palacios, Integrated circuits based on bilayer MoS2 transistors, Nano letters 12 (9) (2012) 4674-4680, doi: https://doi.org/10.1021/nl302015v.

[13] B. Radisavljevic, M. B. Whitwick, A. Kis, Integrated circuits and logic operations based on single-layer MoS2, ACS nano 5 (12) (2011) 9934-9938, doi:https://doi.org/10.1021/nn203715c.

[14] Q. Zhang, X.-F. Wang, S.-H. Shen, Q. Lu, X. Liu, H. Li, J. Zheng, C.-P. Yu, X. Zhong, L. Gu, et al., Simultaneous synthesis and integration of two-dimensional electronic components, Nature Electronics 2 (4) (2019) 164- 170, doi:https://doi.org/10.1038/s41928-019-0233-2.

[15] C. N. R. Rao, Transition Metal Oxides, Annual Review of Physical Chemistry 40 (1) (1989) 291–326, doi:https://doi.org/10.1146/annurev.pc.40.100189.001451.

[16] I. A. de Castro, R. S. Datta, J. Z. Ou, A. Castellanos-Gomez, S. Sriram, T. Daeneke, K. Kalantarzadeh, Molybdenum Oxides – From Fundamentals to Functionality, Advanced Materials 29 (40) (2017) 1701619, doi:https://doi.org/10.1002/adma.201701619.

[17] J. H. Kim, J. K. Dash, J. Kwon, C. Hyun, H. Kim, E. Ji, G.-H. Lee, van der Waals epitaxial growth of single crystal alpha-MoO3 layers on layered materials growth templates, 2D Materials 6 (1) (2018) 015016, doi:https://doi.org/10.1088/2053-1583/aaedc8.

[18] W. J. Dong, J. Ham, G. H. Jung, J. H. Son, J. L. Lee, Ultrafast laser-assisted synthesis of hydrogenated molybdenum oxides for flexible organic solar cells, J. Mater. Chem. A 4 (2016) 4755–4762, doi:https://doi.org/10.1039/C5TA10032A.

[19] K. Inzani, M. Nematollahi, F. Vullum-Bruer, T. Grande, T. W. Reenaas, S. M. Selbach, Electronic properties of reduced molybdenum oxides, Phys. Chem. Chem. Phys. 19 (2017) 9232–9245, doi:https://doi.org/10.1039/C7CP00644F.

[20] S. Balendhran, S. Walia, H. Nili, J. Z. Ou, S. Zhuiykov, R. B. Kaner, S. Sriram, M. Bhaskaran, K. Kalantarzadeh, Semiconductors: Two-Dimensional Molybdenum Trioxide and Dichalcogenides (Adv. Funct. Mater. 32/2013), Advanced Functional Materials 23 (32) (2013) 3946–3946, doi:https://doi.org/10.1002/adfm.201370159.

[21] C. A. Ellefson, O. Marin-Flores, S. Ha, M. G. Norton, Synthesis and applications of molybdenum (IV) oxide, Journal of Materials Science 47 (5) (2012) 2057–2071, doi:https://doi.org/10.1007/s10853-011-5918-5.

[22] K. Santosh, R. C. Longo, R. Addou, R. M. Wallace, K. Cho, Electronic properties of MoS 2/MoO x interfaces: implications in tunnel field effect transistors and hole contacts, Scientific reports 6 (2016) 33562, doi:https://doi.org/10.1038/srep33562.

[23] Z. Gao, Z. Zhou, D. Tománek, Degenerately Doped Transition Metal Dichalcogenides as Ohmic Homojunction Contacts to Transition Metal Dichalcogenide Semiconductors, ACS

nano 13 (5) (2019) 5103–5111, doi:https://doi.org/10.1021/acsnano.8b08190.

[24] T. Y. Ko, A. Jeong, W. Kim, J. Lee, Y. Kim, J. E. Lee, G. H. Ryu, K. Park, D. Kim, Z. Lee, et al., On-stack two-dimensional conversion of MoS2 into MoO3, 2D Materials 4 (1) (2016) 014003, doi:https://doi.org/10.1088/2053-1583/4/1/014003.

[25] R. Kumar, N. Goel, M. Mishra, G. Gupta, M. Fanetti, M. Valant, M. Kumar, Growth of MoS2–MoO3 hybrid microflowers via controlled vapor transport process for efficient gas sensing at room temperature, Advanced Materials Interfaces 5 (10) (2018) 1800071, doi:https://doi.org/10.1002/admi.201800071.

[26] Y. Guo, P.-C. Shen, C. Su, A.-Y. Lu, M. Hempel, Y. Han, Q. Ji, Y. Lin, E. Shi, E. McVay, et al., Additive manufacturing of patterned 2D semiconductor through recyclable masked growth, Proceedings of the National Academy of Sciences 116 (9) (2019) 3437–3442, doi:https://doi.org/10.1073/pnas.1816197116.

[27] W. Yang, J. Yang, J. J. Byun, F. P. Moissinac, J. Xu, S. J. Haigh, M. Domingos, M. A. Bissett, R. A. Dryfe, S. Barg, 3D Printing of Freestanding MXene Architectures for Current-Collector-Free Supercapacitors, Advanced Materials 31 (37) (2019) 1902725, doi:https://doi.org/10.1002/adma.201902725.

[28] T. J. Fleck, A. K. Murray, I. E. Gunduz, S. F. Son, G. T.-C. Chiu, J. F. Rhoads, Additive manufacturing of multifunctional reactive materials, Additive Manufacturing 17 (2017) 176–182, doi:https://doi.org/10.1016/j.addma.2017.08.008.

[29] C. Muratore, A. Juhl, A. Stroud, D. Wenbi Lai, A. Jawaid, K. Burzynski, J. Dagher, G. Leuty, C. Harsch, S. Kim, et al., Printed biomolecular templates for 2D material patterning, Applied Physics Letters 112 (23) (2018) 233704, doi:https://doi.org/10.1063/1.5032090.

[30] S.-Y. Wu, C. Yang, W. Hsu, L. Lin, 3D-printed microelectronics for integrated circuitry and passive wireless sensors, Microsystems & Nanoengineering 1 (2015) 15013, doi:https://doi.org/10.1038/micronano.2015.13.

[31] C. Muratore, J. J. Hu, B. Wang, M. A. Haque, J. E. Bultman, M. L. Jespersen, P. J. Shamberger, M. E. McConney, R. D. Naguy, A. A. Voevodin, Continuous ultra-thin MoS2 films grown by low-temperature physical vapor deposition, Applied Physics Letters 104 (26) (2014) 261604, doi:https://doi.org/10.1063/1.4885391.

[32] R. H. Kim, J. Leem, C. Muratore, S. Nam, R. Rao, A. Jawaid, M. Durstock, M. McConney, L. Drummy, R. Rai, et al., Photonic crystallization of two-dimensional MoS 2 for stretchable photodetectors, Nanoscale 11 (28) (2019) 13260–13268, doi:https://doi.org/10.1039/C9NR02173F.

[33] R. A. Vilá, R. Rao, C. Muratore, E. Bianco, J. A. Robinson, B. Maruyama, N. R. Glavin, In situ crystallization kinetics of two-dimensional MoS2, 2D Materials 5 (1) (2017) 011009, doi:https://doi.org/10.1088/2053-1583/aa9674.

[34] A. Kumar, E. Villarreal, X. Zhang, E. Ringe, Micro-Extinction Spectroscopy (MExS): a versatile optical characterization technique, Advanced Structural and Chemical Imaging 4 (1) (2018) 8, doi:https://doi.org/10.1186/s40679-018-0057-6.

[35] L. Wang, G.-h. Zhang, J. Dang, K.-c. Chou, Oxidation roasting of molybdenite concentrate, Transactions of Nonferrous Metals Society of China 25 (12) (2015) 4167–4174, doi:https://doi.org/10.1016/S1003-6326(15)64067-5.

[36] Y. Shigegaki, S. Basu, M. Wakihara, M. Taniguchi, Thermal analysis and kinetics of oxidation of molybdenum sulfides, Journal of Thermal Analysis and Calorimetry 34 (5-6) (1988) 1427–1440, doi:https://doi.org/10.1007/BF01914367.

[37] R. F. Sebenik, A. R. Burkin, R. R. Dorfler, J. M. Laferty, G. Leichtfried, H. Meyer-Grünow, P. C. H. Mitchell, M. S. Vukasovich, D. A. Church, G. G. Van Riper, J. C. Gilliland, S. A. Thielke, Molybdenum and Molybdenum Compounds, American Cancer Society, 2000, ISBN 9783527306732, doi:https://doi.org/10.1002/14356007.a16_655.

[38] I. Wilkomirsky, A. Otero, E. Balladares, Kinetics and Reaction Mechanisms of High-Temperature Flash Oxidation of Molybdenite, Metallurgical and Materials Transactions B 41 (1) (2010) 63–73, ISSN 1073-5615, 1543-1916, doi:https://doi.org/10.1007/s11663-009-9313-4.

[39] C. Muratore, J. E. Bultman, S. M. Aouadi, A. A. Voevodin, In situ Raman spectroscopy for examination of high temperature tribological processes, Wear 270 (3-4) (2011) 140–145, doi:https://doi.org/10.1016/j.wear.2010.07.012.

[40] T. Marin, T. Utigard, C. Hernandez, Roasting Kinetics of Molybdenite Concentrates, Canadian Metallurgical Quarterly 48 (1) (2009) 73–80, ISSN 0008-4433, 1879-1395, doi:https://doi.org/10.1179/cmq.2009.48.1.73.

[41] L. Wang, G.-h. Zhang, J. Dang, K.-c. Chou, Oxidation roasting of molybdenite concentrate, Transactions of Nonferrous Metals Society of China 25 (12) (2015) 4167–4174, ISSN 10036326, doi:https://doi.org/10.1016/S1003-6326(15)64067-5.

[42] M. E. McConney, N. R. Glavin, A. T. Juhl, M. H. Check, M. F. Durstock, A. A. Voevodin, T. E. Shelton, J. E. Bultman, J. Hu, M. L. Jespersen, et al., Direct synthesis of ultra-thin large area transition metal dichalcogenides and their heterostructures on stretchable polymer surfaces, Journal of Materials Research 31 (7) (2016) 967–974, doi:https://doi.org/10.1557/jmr.2016.36.

[43] M. Dieterle and G. Mestl, Raman spectroscopy of molybdenum oxides, Physical Chemistry Chemical Physics 4 (5) (2002) 822-826, doi:https://doi.org/10.1039/b107046k.

[44] J. Blumm, J. Opfermann, Improvement of the mathematical modeling of flash measurements, High Temperatures. High Pressures 34 (5) (2002) 515–521, doi:https://doi.org/10.1068/htjr061.

[45] R. T. Bell, A. G. Jacobs, V. C. Sorg, B. Jung, M. O. Hill, B. E. Treml, M. O. Thompson, Lateral Temperature-Gradient Method for High-Throughput Characterization of Material Processing by Millisecond Laser Annealing, ACS Combinatorial Science 18 (9) (2016) 548–558, ISSN 2156-8952, 2156-8944, doi:https://doi.org/10.1021/acscombsci.6b00043.

[46] M. Yu, X. Cheng, Y. Zeng, Z. Wang, Y. Tong, X. Lu, S. Yang, Dual-Doped Molybdenum Trioxide Nanowires: A Bifunctional Anode for Fiber-Shaped Asymmetric Supercapacitors and Microbial Fuel Cells, Angewandte Chemie International Edition 55 (23) (2016) 6762–

6766, ISSN 14337851, doi:https://doi.org/10.1002/anie.201602631.

[47] S. Shin, Z. Jin, D. H. Kwon, R. Bose, Y.-S. Min, High Turnover Frequency of Hydrogen Evolution Reaction on Amorphous MoS 2 Thin Film Directly Grown by Atomic Layer Deposition, Langmuir 31 (3) (2015) 1196–1202, ISSN 0743-7463, 1520-5827, doi:https://doi.org/10.1021/la504162u.

[48] O. de Melo, Y. González, A. Climent-Font, P. Galán, A. Ruediger, M. Sánchez, C. Calvo-Mola, G. Santana, V. Torres-Costa, Optical and electrical properties of MoO2 and MoO3 thin films prepared from the chemically driven isothermal close space vapor transport technique, Journal of Physics: Condensed Matter 31 (29) (2019) 295703, ISSN 0953-8984, 1361-648X, doi:https://doi.org/10.1088/1361-648X/ab18e2.

[49] D. Manno, M. D. Giulio, A. Serra, T. Siciliano, G. Micocci, Physical properties of sputtered molybdenum oxide thin films suitable for gas sensing applications, Journal of Physics D: Applied Physics 35 (3) (2002) 228–233, doi:https://doi.org/10.1088/0022-3727/35/3/310.

[50] L. Lajaunie, F. Boucher, R. Dessapt, P. Moreau, Strong anisotropic influence of local-field effects on the dielectric response of α-MoO3, Phys. Rev. B 88 (2013) 115141, doi:https://doi.org/10.1103/PhysRevB.88.115141.

[51] D. Roy, J. H. Klootwijk, N. A. M. Verhaegh, H. H. A. J. Roosen, R. A. M. Wolters, Comb Capacitor Structures for On-Chip Physical Uncloneable Function, IEEE Transactions on Semiconductor Manufacturing 22 (1) (2009) 96–102, ISSN 0894-6507, doi:https://doi.org/10.1109/TSM.2008.2010738.

[52] J. Park, J. Mun, J. Shin, S. Kang, Highly sensitive two-dimensional MoS2 gas sensor decorated with Pt nanoparticles, Royal Society Open Science, 5, 181462, doi: https://doi.org/10.1098/rsos.181462.

[53] T. Pham, G. Li, E. Bekyarova, M. Itkis, A. Mulchandani, MoS2-based optoelectronic gas sensor with sub parts-per-billion limit of NO2 gas detection, ACS Nano 13 (3) (2019) 3196-3205, https://doi.org/10.1021/acsnano.8b08778.

[54] T. Järvinen, G. S. Lorite, J. Peräntie, G. Toth, S. Saarakkala, V. K. Virtanen, K. Kordas, WS2 and MoS2 thin film gas sensors with high response to NH3 in air at low temperature, Nanotechnology 30 (40) (2019) 405501, doi:https://doi.org/10.1088/1361-6528/ab2d48.

[55] S. K. Saha, D. Wang, V. H. Nguyen, Y. Chang, J. S. Oakdale, S.-C. Chen, Scalable submicrometer additive manufacturing, Science 366 (6461) (2019) 105–109, doi: https://doi.org/10.1126/science.aax8760.

[56] P. Ghildiyal, Y. Yang, D. J. Kline, S. Holdren, M. R. Zachariah, Ultrafast, scalable laser photothermal synthesis and writing of uniformly dispersed metal nanoclusters in polymer films, Nanoscale 11 (28) (2019) 13354–13365, doi:https://doi.org/10.1039/C9NR02839K.

[57] M. Shusteff, A. E. Browar, B. E. Kelly, J. Henriksson, T. H. Weisgraber, R. M. Panas, N. X. Fang, C. M. Spadaccini, One-step volumetric additive manufacturing of complex polymer structures, Science advances 3 (12) (2017) eaao5496, doi:https://doi.org/10.1126/sciadv.aao5496.